第 50 卷 第 18 期/2023 年 9 月/中国激光　研究论文

中国激光

空穴主导雪崩倍增的短波长SiC紫外单光子探测器

苏琳琳，杨成东*

无锡学院电子信息工程学院，江苏 无锡 214105

摘要　制备并分析了SiC nip雪崩光电二极管（APDs）雪崩倍增的物理机制。与280 nm紫外光相比，在240 nm紫外光入射时，SiC nip APD表现出更高的增益和更大的单光子探测效率。在240 nm紫外光入射时，SiC nip APD表现为空穴主导碰撞离化过程，随着入射光波长增加到280 nm，电子和空穴共同主导碰撞离化过程。由于SiC中空穴的碰撞离化系数大于电子，空穴主导的碰撞离化过程将具有更大的光子雪崩概率和更高的增益。因此，得益于空穴主导雪崩倍增过程，SiC nip APD更适用于短波长紫外光探测。

关键词　激光器；SiC；雪崩光电二极管；深紫外光探测；光子雪崩概率

中图分类号　O475　　**文献标志码**　A　　**DOI**：10.3788/CJL221289

1　引　　言

微弱紫外光探测在火灾预警、电晕检测、导弹尾焰检测、深空检测和紫外通信等领域中具有广泛的应用[1-7]。雪崩光电二极管（APDs）具有便于集成的优势，其量子效率和增益水平也远高于光电倍增管，是目前备受关注的一种微弱光探测器[8-9]。SiC作为一种宽禁带半导体材料，光响应截止波长位于380 nm附近，具有可见光盲特性，能够有效屏蔽环境中可见光和红外光的背景噪声[10]。此外，得益于SiC在功率器件领域的广泛应用，SiC的外延生长和微制造工艺日趋成熟，低材料缺陷密度和成熟的器件制备工艺加速了SiC APD的快速发展。

SiC APD多设计为pn结结构，根据外延层分布可分为pin APD和nip APD，其外延结构从上向下分别为p+接触层、p过渡层、i雪崩层、n型接触层和n+接触层、n过渡层、i雪崩层、p型接触层/n型接触层[11-13]。SiC APD在进行微弱光探测时，器件工作在高压雪崩击穿状态下，SiC pin和nip APD表现出完全相反的电子和空穴漂移方向：pin APD中的空穴向p型层即器件表面漂移，电子向n型层即衬底漂移，nip APD则与之相反。光生载流子的雪崩倍增过程发生在i雪崩层，即APD通过雪崩层中电子空穴的碰撞离化过程来实现对微弱光的放大。Cha等[14]估算了SiC在室温下的吸收系数，结果表明SiC对高能量光子表现出更大的吸收系数。随着入射紫外光波长的增加，光子能量降低，光生电子空穴的产生位置将逐渐从器件表面向器件深处扩展。因此，对于SiC pin和nip APD，由于载流子漂移方向的差异，在进行不同波长紫外光探测时，引发碰撞离化的载流子类型可能不同。由于SiC中空穴的碰撞离化系数比电子大，不同的碰撞离化载流子类型势必会影响器件的探测性能。尽管优异性能的SiC pn结型APD已经被成功制备，但关于器件雪崩行为的本质研究还鲜有讨论。本文设计并制备了SiC nip APD，器件对短波长紫外光表现出更高的单光子探测效率，这得益于空穴主导的碰撞离化过程。研究结果有利于SiC APD工作机制的深入理解，并为今后SiC APD器件的优化提供了理论指导。

2　器件制备

器件制备在n型4H-SiC衬底上，如图1所示，器件外延结构由下而上分别为一层10 μm厚的p型接触层（受主掺杂浓度$N_\mathrm{A}=3\times10^{18}$ cm^{-3}），一层0.05 μm厚的i过渡层，一层0.7 μm厚的n−雪崩倍增层（施主掺杂浓度$N_\mathrm{D}=1\times10^{15}$ cm^{-3}），一层0.2 μm厚的n型过渡层（施主掺杂浓度$N_\mathrm{D}=1\times10^{18}$ cm^{-3}）和一层0.15 μm厚的n+接触层（施主掺杂浓度$N_\mathrm{D}=1\times10^{19}$ cm^{-3}）。器件制备的第一步是台面刻蚀。为了抑制台面边缘电场，器件设计为倾斜台面结构，采用光刻胶回流技术形成倾斜台面以刻蚀掩膜，然后利用感应耦合等离子体刻蚀系统对外延片进行刻蚀，刻蚀深度为0.5 μm，倾斜角度为5°，器件直径为150 μm，估算的填充因子约为90%[13]。为了修复表面刻蚀损伤、降低表面漏电流，我们对刻蚀后的外延片进行表面钝化处理[13]：首先将外延片在高温管式炉中氧化1 h并用氢氟酸溶液对氧化层进行腐蚀，然后将外延片在高温管式炉中氧化3 h，

收稿日期：2022-09-30；**修回日期**：2022-10-29；**录用日期**：2022-11-28；**网络首发日期**：2022-12-08

基金项目：国家自然科学基金（62106111）、无锡学院引进人才科研启动专项经费（2021r011，2021r012）

通信作者：*860118@cwxu.edu.cn

最后利用等离子体增强化学气相沉积法生长 1 μm 厚的 SiO$_2$。器件制备的最后一个环节是制备欧姆电极：在对外延片进行光刻显影后，采用氢氟酸溶液腐蚀掉钝化层，获得正面 n 型电极窗口；外延片被放置在电子束蒸发系统中进行电极蒸镀，正面和背面的 n 型电极均采用 Ni/Ti/Al/Au 金属层；利用快速热退火系统，将外延片在 850 ℃氮气氛围下退火 3 min。

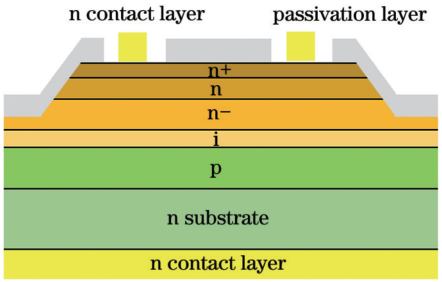

图 1　SiC nip APD 的剖面结构示意图

Fig. 1　Structural diagram of cross section of SiC nip APD

3　分析与讨论

图 2 为 SiC nip APD 在室温下的电流-电压和增益曲线。在雪崩击穿之前，器件的暗电流低于 pA 量级。随着电压增加到一定水平，器件暗电流和光电流急剧上升，此时器件处于雪崩击穿状态，能够进行微弱紫外光探测。若把器件增益达到 1000 时的电压值定义为击穿电压，那么器件击穿电压为 260 V。当过偏压为 4 V 时，器件增益达到 1.5×10^6。

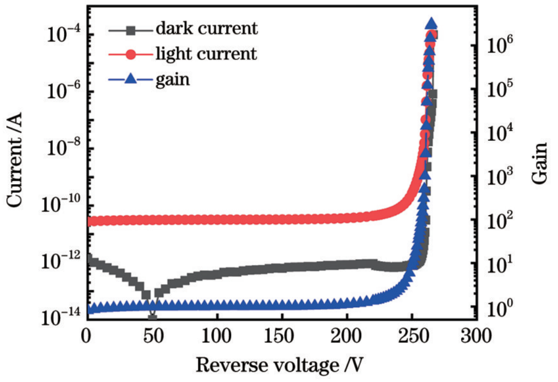

图 2　SiC nip APD 的电流-电压和增益曲线

Fig. 2　Current-voltage and gain curves of SiC nip APD

为了研究 SiC nip APD 的雪崩机制，我们详细测量了器件在 220～320 nm 入射紫外光下的增益曲线，如图 3(a)所示。随着入射光波长的增加，器件增益曲线向高电压方向移动，即高能量紫外光入射时，器件的击穿电压更低。提取了 SiC nip APD 在不同入射紫外光波长下的击穿电压(V_B)相对于 220 nm 时击穿电压(V_B')的变化情况，如图 3(b)所示。当入射紫外光波长从 220 nm 增加到 320 nm 时，器件的击穿电压增加了 1.3 V。这说明在相同的电压下，高能量紫外光入射时 SiC nip APD 的增益行为较显著，意味着此时在耗尽区中发生了更强烈的光生载流子碰撞离化过程，有助于进行短波长紫外光探测。

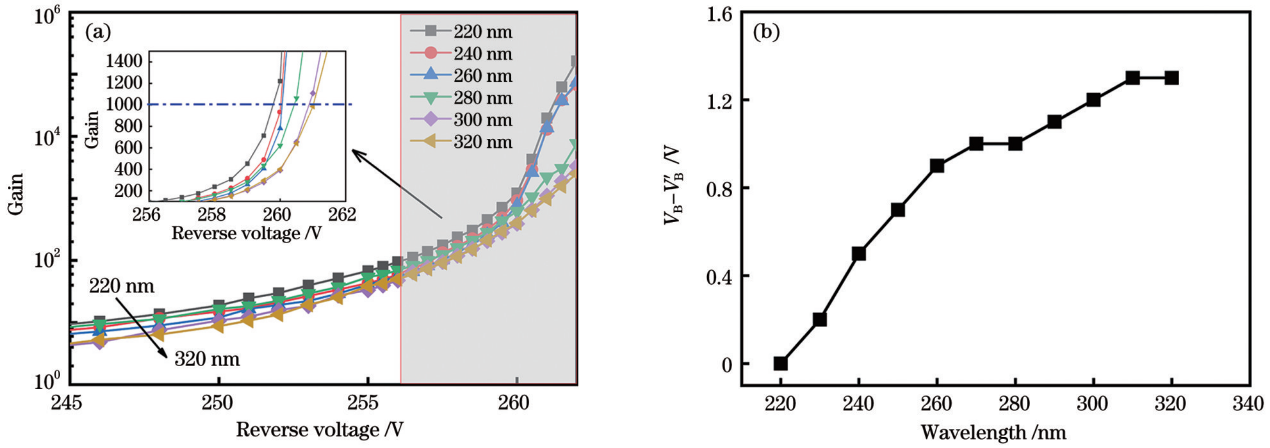

图 3　SiC nip APD 在 220～320 nm 入射紫外光下的雪崩特性。(a)增益曲线；(b)击穿电压

Fig. 3　Avalanche characteristics of SiC nip APD under 220–320 nm incident ultraviolet light . (a) Gain curves; (b) breakdown voltage

为了进一步证明 SiC nip APD 在高能量光子入射时具有更强的载流子碰撞离化过程，我们对器件的单光子探测效率(SPDE)进行了研究。单光子探测效率是评价微弱紫外光探测性能的一个关键参数，直接反映一个入射光子被探测到的可能性。我们利用图 4(a)所示的被动淬灭电路表征 SiC nip APD 的暗计数和光计数并计算单光子探测效率[15]。采用源表为 APD 施加高于击穿电压的工作电压，使器件处于雪崩倍增状态。APD 与一个 50 kΩ 的淬灭电阻(R_L)串联用于对雪崩电流的快速淬灭，同时与一个 100 Ω 的取样电阻(R_S)串联用于雪崩电压脉冲信号的提取，一台示波器和一台光子计数器与取样电阻并联以观测雪崩电压脉冲信号输出。采用 240 nm 和 280 nm 发光二极管(LED)表征 APD 光计数水平，源表为 LED 提供驱动电流。采用一个光响应度已知的商用硅基紫外增强光电探测器标定 APD 入射光子数，经过估算，240 nm 和 280 nm 光子入射频率均为 5×10^6 /s。图 4(b)为 SiC APD 在被动淬灭电路中的一个典型雪崩电压脉冲信

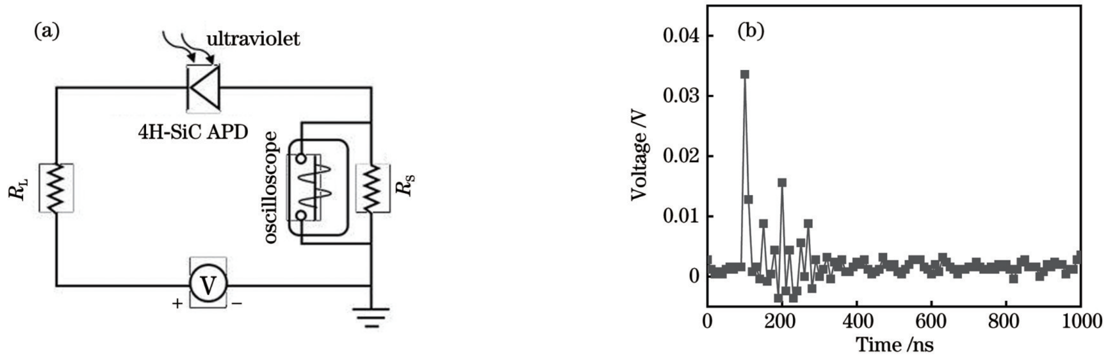

图4 SiC APD探测能力表征。(a)被动淬灭电路；(b)一个典型的雪崩电压脉冲信号

Fig. 4 Characterization of SiC APD detection capability. (a) Passive quenching circuit; (b) one typical avalanche voltage pulse signal

号，脉冲高度为34 mV。当APD外加高于击穿电压的反向电压时，器件中的载流子在高电场强度的作用下发生碰撞离化，产生雪崩电压脉冲信号，我们将暗载流子和光生载流子引起的脉冲信号计数频率值分别称为暗计数率（DCR）和光计数率（PCR）。APD的单光子探测效率计算公式为

$$S_{\mathrm{PDE}}=\frac{P_{\mathrm{CR}}-D_{\mathrm{CR}}}{n}\times 100\%=F_{\mathrm{f}}\times P_{\mathrm{AP}}\times Q_{\mathrm{E}}, \quad (1)$$

式中：S_{PDE}为单光子探测效率；P_{CR}为光计数率；D_{CR}为暗计数率；n为入射到器件表面的光子流密度；F_{f}为器件的填充因子；P_{AP}为光子雪崩概率，即光生载流子发生雪崩倍增的可能性；Q_{E}为0 V时器件的量子效率。图5为SiC nip APD在240 nm和280 nm入射紫外光波长下的暗计数-单光子探测效率曲线。当过偏压为3 V时，暗计数为1.7 Hz/μm^2，器件对240 nm和280 nm紫外光的探测效率分别为11.4%和6.5%。在相同的工作条件下，SiC nip APD对短波长紫外光的单光子探测效率显然更高。

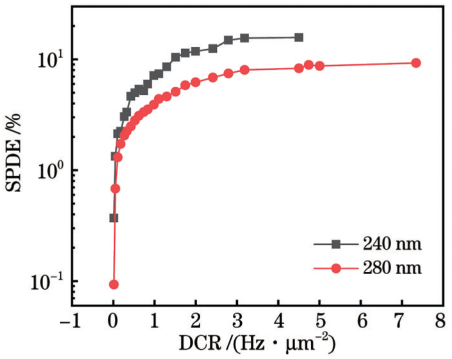

图5 240 nm和280 nm入射紫外光下SiC nip APD的暗计数-单光子探测效率曲线

Fig. 5 Dark count rate versus single photon detection efficiency for SiC nip APD under 240 nm and 280 nm incident UV light

根据式（1），APD的单光子探测效率与量子效率和光子雪崩概率成正比。因此，我们首先表征了SiC nip APD在0 V下的光响应曲线，如图6所示。器件在285 nm处的光响应峰值为0.115 A/W，对应最大量子效率为50%。当入射紫外光波长为240 nm和280 nm时，量子效率分别为15%和45%，假设SiC nip APD工作在3 V过偏压条件下，估算的光子雪崩概率分别为84%和16%。由此可见，SiC nip APD对高能量紫外光表现出更大的单光子探测效率，这主要是因为短波长光子具有大的光子雪崩概率，进一步说明高能量紫外光入射时器件耗尽区中发生了更强烈的光生载流子碰撞离化过程。

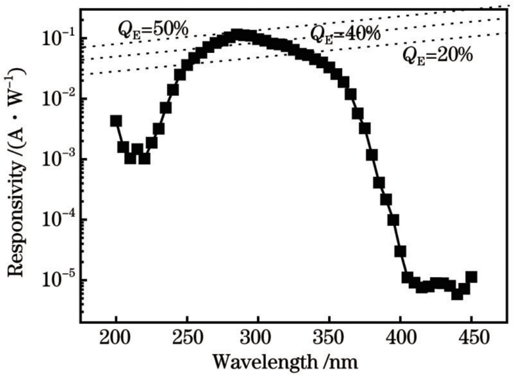

图6 SiC nip APD的光响应曲线

Fig. 6 Optical response curve of SiC nip APD

为了从器件本质上解释光子雪崩概率的差异性，我们对光照下器件的雪崩电压脉冲高度进行了分析。图7给出了过偏压为3 V时SiC nip APD在240 nm和280 nm入射紫外光下的雪崩电压脉冲高度分布统计。可以看出，器件在进行高能量紫外光探测时雪崩电压脉冲高度更大，在240 nm和280 nm入射紫外光下，50 mV以上的雪崩电压脉冲高度分别为10%和4%。一个大的雪崩电压脉冲高度意味着一个光生载流子在耗尽区中经历了强烈的雪崩倍增过程。Cha等[14]根据光响应谱线估算了4H-SiC在室温下的吸收系数，对于240 nm和280 nm紫外光，估算的4H-SiC吸收系数分别为2×10^5/cm和7×10^3/cm，经计算240 nm和280 nm紫外光在4H-SiC中的透射深度分别为50.0 nm和1.4 μm。当240 nm紫外光入射到SiC nip APD表面时，光生载流子在器件上表面产生并通过扩散运动进入耗尽区。在反向偏压作用下，空穴一旦进入耗尽区

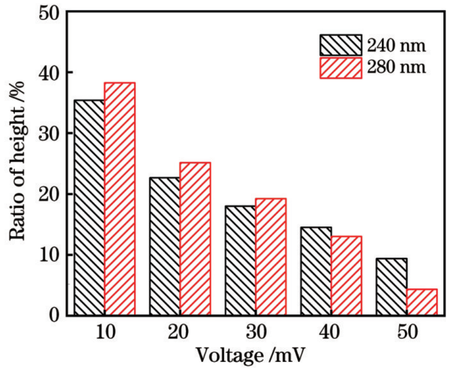

图 7 240 nm 和 280 nm 入射紫外光下 SiC nip APD 的雪崩电压脉冲高度分布

Fig. 7 Avalanche voltage pulse height distributions of SiC nip APD under 240 nm and 280 nm incident UV light

便在强电场的作用下向衬底作漂移运动，其加速距离和碰撞离化过程会跨越整个耗尽区；而电子在进入耗尽区后会向器件表面作漂移运动，加速距离和碰撞离化过程则可以忽略不计，此时，器件的雪崩过程由空穴主导[16]。当 280 nm 紫外光入射到 SiC nip APD 表面时，1.4 μm 的透射深度穿过耗尽区，电子和空穴均发生了雪崩倍增过程。由于 SiC 中空穴的碰撞离化系数大于电子[17-19]，因此在 240 nm 紫外光入射时，空穴主导的碰撞离化过程使器件表现出更高的单光子探测效率。一个 240 nm 光子产生的光生空穴在大的加速距离和碰撞离化距离及高的碰撞离化系数下将会发生强烈的碰撞离化过程，雪崩电压脉冲信号的幅值也较大。大的碰撞离化系数决定了空穴主导的碰撞离化过程表现出大的光子雪崩概率和高的雪崩增益。得益于空穴主导碰撞离化过程，SiC nip APD 更适用于短波长紫外光探测。

4 结 论

设计并制备了 SiC nip APD 并对其雪崩的本质特性进行了详细研究。在高能量紫外光入射下，SiC nip APD 的雪崩倍增过程由空穴主导；随着入射光波长的增加，空穴对雪崩倍增过程的贡献逐渐减少，而电子的贡献逐渐增加。由于 SiC 中空穴的碰撞离化系数比电子大，空穴主导的碰撞离化过程更容易发生雪崩倍增，因此 SiC nip APD 对高能量紫外光表现出更高的增益和更大的单光子探测效率。SiC nip APD 的本质特性决定了器件更适用于短波长紫外光探测，特别是在 240～280 nm 的日盲波段，器件既可以屏蔽太阳辐射的影响，又可以最大程度发挥单光子探测效率的优势。

参 考 文 献

[1] Chen H Y, Liu K W, Hu L F, et al. New concept ultraviolet photodetectors[J]. Materials Today, 2015, 18(9): 493-502.

[2] Wang Y, Qian Y S, Kong X Y. Photon counting based on solar-blind ultraviolet intensified complementary metal-oxide-semiconductor (ICMOS) for corona detection[J]. IEEE Photonics Journal, 2018, 10(6): 7000919.

[3] 赵太飞，李永明，袁麓 . 装甲编队无线紫外光隐秘通信的中继选择研究[J]. 光电工程，2019，46(5): 63-70.
Zhao T F, Li Y M, Yuan L. Research on relay selection of armored formations wireless UV covert communication[J]. Opto-Electronic Engineering, 2019, 46(5): 63-70.

[4] 袁兆林，胡育杰，吕季辉，等 . ZnO 纳米线阵列/PVK 异质结紫外光探测器特性[J]. 光学学报，2022，42(22): 2204001.
Yuan Z L, Hu Y J, Lü J H, et al. Characteristics of ZnO nanowire arrays/PVK heterojunction ultraviolet photodetector[J]. Acta Optica Sinica, 2022, 42(22): 2204001.

[5] 杨成东，夏开鹏，马文烨，等 . 高耐压和低暗计数 SiC 紫外雪崩光电二极管[J]. 光学学报，2023，43(3): 0304001.
Yang C D, Xia K P, Ma W Y, et al. High overbias tolerance and low dark count rate SiC UV avalanche photodiodes[J]. Acta Optica Sinica, 2023, 43(3): 0304001.

[6] 王江，罗林保 . 基于氧化镓日盲紫外光电探测器的研究进展[J]. 中国激光，2021，48(11): 1100001.
Wang J, Luo L B. Advances in Ga$_2$O$_3$-based solar-blind ultraviolet photodetectors[J]. Chinese Journal of Lasers, 2021, 48(11): 1100001.

[7] 赵忆睿，曹念文，贾鹏程，等 . 紫外多波长激光雷达的臭氧和气溶胶同步观测研究[J]. 激光与光电子学进展，2022，59(16): 1601001.
Zhao Y R, Cao N W, Jia P C, et al. Simultaneous observation of ozone and aerosol by ultraviolet multi-wavelength lidar[J]. Laser & Optoelectronics Progress, 2022, 59(16): 1601001.

[8] 陈勇强，贺岩，罗远，等 . 基于盖革 APD 阵列脉冲式三维成像激光雷达系统[J]. 中国激光，2023，50(2): 0210001.
Chen Y Q, He Y, Luo Y, et al. Pulsed three dimensional imaging lidar system based on Geiger-mode APD array[J]. Chinese Journal of Lasers, 2023, 50(2): 0210001.

[9] Yi X, Xie S Y, Liang B L, et al. Extremely low excess noise and high sensitivity AlAs$_{0.56}$Sb$_{0.44}$ avalanche photodiodes[J]. Nature Photonics, 2019, 13(10): 683-686.

[10] Powell A R, Rowland L B. SiC materials-progress, status, and potential roadblocks[J]. Proceedings of the IEEE, 2002, 90(6): 942-955.

[11] Su L L, Zhou D, Liu Q, et al. Effect of a single threading dislocation on electrical and single photon detection characteristics of 4H-SiC ultraviolet avalanche photodiodes[J]. Chinese Physics Letters, 2020, 37(6): 068502.

[12] Li L H, Zhou D, Lu H, et al. 4H-SiC avalanche photodiode linear array operating in Geiger mode[J]. IEEE Photonics Journal, 2017, 9(5): 1-7.

[13] Su L L, Zhou D, Lu H, et al. Recent progress of SiC UV single photon counting avalanche photodiodes[J]. Journal of Semiconductors, 2019, 40(12): 65-75.

[14] Cha H Y, Sandvik P M. Electrical and optical modeling of 4H-SiC avalanche photodiodes[J]. Japanese Journal of Applied Physics, 2008, 47(7): 5423-5425.

[15] Zhou X Y, Tan X, Lü Y J, et al. Single-photon-counting performance of 4H-SiC avalanche photodiodes with a wide-range incident flux[J]. IEEE Photonics Technology Letters, 2020, 32(14): 847-850.

[16] Su L L, Xu W Z, Zhou D, et al. Avalanche mechanism analysis of 4H-SiC n-i-p and p-i-n avalanche photodiodes working in Geiger mode[J]. Chinese Optics Letters, 2021, 19(9): 092501.

[17] Bellotti E, Nilsson H E, Brennan K F, et al. Monte Carlo calculation of hole initiated impact ionization in 4H phase SiC[J]. Journal of Applied Physics, 2000, 87(8): 3864-3871.

[18] Konstantinov A, Neyer T. Pattern of near-uniform avalanche breakdown in off-oriented 4H SiC[J]. IEEE Transactions on Electron Devices, 2014, 61(12): 4153-4157.

[19] Loh W S, Ng B K, Ng J S, et al. Impact ionization coefficients in 4H-SiC[J]. IEEE Transactions on Electron Devices, 2008, 55(8): 1984-1990.

Short-Wavelength SiC Ultraviolet Single Photon Detector Based on Hole-Dominated Avalanche Multiplication

Su Linlin, Yang Chengdong*

School of Electronic Information Engineering, Wuxi University, Wuxi 214105, *Jiangsu, China*

Abstract

Objective SiC avalanche photodiodes (APDs) have the merits of visible light blindness, low weight, and high gain, exhibiting obvious advantages in weak ultraviolet detection. SiC APDs are mostly designed as pn junction structures, which can be divided into pin and nip APDs, according to the distribution of the epitaxial layers. When the SiC APD is conducting weak light detection, the device works under the avalanche state; the SiC pin and nip APDs exhibit completely opposite carrier drift directions. Holes in the pin APD drift toward the p-type layer, that is, the device surface, whereas the electrons drift toward the n-type layer, that is, the substrate; the nip APD exhibits the opposite. Cha et al. estimated the absorption coefficient of SiC at room temperature, and the results showed that SiC has a higher absorption coefficient for high-energy photons. Therefore, for the SiC pin and nip APDs, owing to the difference of the carrier drift direction, the types of carriers that cause collision ionization may be different for different wavelength detections . Considering that the collision ionization coefficient of holes in SiC is larger than that of electrons, different types of collision ionization carriers will certainly affect the detection performance of APDs. In this work, SiC nip APDs are designed and fabricated with a higher single photon detection efficiency for short wavelength ultraviolet light, benefitting from the hole dominated collision ionization process. This work is conducive for the in-depth understanding of the working mechanism of SiC APD and provides theoretical guidance for its optimization in the future.

Methods The SiC nip APD is fabricated on an n-type 4H-SiC substrate (Fig. 1). The epitaxial structure is a 10 μm thick p-type contact layer (acceptor doping concentration $N_A=3\times10^{18}$ cm^{-3}), a 0.05 μm thick transition layer, a 0.7 μm thick n-type avalanche multiplication layer (donor doping concentration $N_D=1\times10^{15}$ cm^{-3}), a 0.2 μm thick n-type transition layer ($N_D=1\times10^{18}$ cm^{-3}), and a 0.15 μm thick n-type contact layer ($N_D=1\times10^{19}$ cm^{-3}) from bottom to top. The first step of APD fabrication is mesa etching. To suppress the peak electric field at the edge of mesa, the device is designed to be a beveled mesa structure (beveled angle of ~5°), and the etching depth is 0.5 μm. The epitaxial wafer is then passivated by the thermal oxidation layer and the plasma-enhanced chemical vapor deposition SiO_2 layer. Finally, both the front and back contact metals (Ni/Ti/Al/Au) are deposited by electron-beam evaporation and annealed by rapid thermal annealing at 850 ℃ for 3 min in N_2 ambience.

Results and Discussions To study the avalanche mechanism of SiC nip APD, the gain curves of SiC nip APD are plotted (Fig. 3). When the wavelength of the incident ultraviolet light increases from 220 nm to 320 nm, the breakdown voltage of the nip APD increases by 1.3 V. When the over bias is 3 V, the dark count rate is 1.7 Hz/μm^2, and the single photon detection efficiency of the SiC nip APD for 240 nm and 280 nm incident UV light is 11.4% and 6.5%, respectively (Fig. 5). In the same working conditions, the single photon detection efficiency of the SiC nip APD for short wavelength ultraviolet light is evidently higher. The quantum efficiency of the SiC nip APD under 240 nm and 280 nm incident UV light is 15% and 45%, respectively (Fig. 6). Assuming that the SiC nip APD operates at 3 V overbias, the estimated photon avalanche probability is 84% and 16% at 240 nm and 280 nm illumination, respectively. It can be observed that the high single photon detection efficiency of the SiC nip APD for high-energy ultraviolet light is mainly related to the large photon avalanche probability. When the 240 nm ultraviolet light is incident on the SiC nip APD surface, photogenerated carriers are generated on the device surface and enter the depletion region through diffusion. Under the avalanche state, when the hole enters the depletion region, it drifts towards the substrate under the strong electric field, and its acceleration distance and collision ionization process span the entire depletion region. When the electrons drift towards the device surface after entering the depletion region, the acceleration distance and collision ionization process can be ignored. Thus, at 240 nm illumination, the avalanche process of the SiC nip APD is dominated by holes. With the increase of the ultraviolet light wavelength, the contribution of the electrons gradually increases. The collision ionization coefficient of holes in SiC is larger than that of electrons; therefore, the hole-dominated collision ionization process exhibits a higher avalanche gain and higher single photon detection efficiency.

Conclusions In this work, SiC nip APDs are designed, and their avalanche characteristics are studied in detail. Under high energy ultraviolet light illumination, the avalanche multiplication process of the SiC nip APD is dominated by holes. With the increase of the incident light wavelength, the contribution of the electrons gradually increases. As the collision ionization coefficient of holes in SiC is larger than that of electrons, the SiC nip APD exhibits a higher gain and higher single photon detection efficiency for high-energy ultraviolet light illumination. The essential characteristics of the SiC nip APD ensure that the device is more suitable for short wavelength ultraviolet detection.

Key words lasers; SiC; avalanche photodiode; deep ultraviolet detection; photon avalanche probability